
**BNL-112729-2016-JA**

# Explore the Effects of Microstructural Defects on Voltage Fade of Li- and Mn-Rich Cathodes

**Enyuan Hu, Yingchun Lyu, Huolin L. Xin, Jue Liu, Lili Han, Seong-Min Bak, Jianming Bai, Xiqian Yu, Hong Li, Xiao-Qing Yang**

*Submitted to Nano Letters*

May 2016

**Center for Functional Nanomaterials**

**Brookhaven National Laboratory**

**U.S. Department of Energy**
**USDOE Office of Science (SC),**
**Basic Energy Sciences (BES) (SC-22)**

# DISCLAIMER

# Explore the Effects of Microstructural Defects on Voltage Fade of Li- and Mn-Rich Cathodes

Enyuan Hu[†], Yingchun Lyu[§¶], Huolin L. Xin[‡], Jue Liu[†], Lili Han[‡], Seong-Min Bak[†], Jianming Bai[‖], Xiqian Yu[†§*], Hong Li[§*], Xiao-Qing Yang[†*]

[†]Department of Chemistry, Brookhaven National Laboratory, Upton, NY 11973, United States

[§]Beijing National Laboratory for Condensed Matter Physics, Institute of Physics, Chinese Academy of Sciences, Beijing, 100190, P. R. China

¶Materials Genome Institute, Shanghai University, Shanghai 200444, China

[‡]Center for Functional Nanomaterials, Brookhaven National Laboratory, Upton, New York 11973, United States

[‖]National Synchrotron Light Source II, Brookhaven National Laboratory, Upton, New York 11973, United States

Key words: lithium-ion battery, voltage fade, microstructural defect, prelithiation

**Abstract:** Li- and Mn-rich (LMR) cathode materials have been considered as promising candidates for energy storage applications due to high energy density. However, these materials suffer from a serious problem of voltage fade. Oxygen loss and the layer to spinel phase transition are two major contributors of such voltage fade. In this paper, using a combination of x-ray diffraction (XRD), pair distribution function (PDF), x-ray absorption (XAS) techniques and aberration-corrected scanning transmission electron microscopy (STEM), we studied the effects of micro structural defects, especially the grain boundaries on the oxygen loss and layered-to-spinel phase transition through prelithiation of a model compound $Li_2Ru_{0.5}Mn_{0.5}O_3$. It

is found that the nano-sized micro structural defects, especially the large amount of grain boundaries created by the prelithiation can greatly accelerate the oxygen loss and voltage fade. Defects (such as nano-sized grain boundaries) and oxygen release form a positive feedback loop, promote each other during cycling, and accelerate the two major voltage fade contributors: the transition metal reduction and layered-to-spinel phase transition. These results clearly demonstrate the important relationships among the oxygen loss, microstructural defects and voltage fade. The importance of maintaining good crystallinity and protecting the surface of LMR material are also suggested.

## Introduction

A great deal of research efforts have been devoted to the study of Li- and Mn-rich (LMR) cathode materials since they were reported[1-4]. Commonly denoted as $x\mathrm{Li_2MnO_3}\cdot(1\text{-}x)\mathrm{LiMO_2}$ (M = transition metal cations), these materials can provide reversible capacities greater than 280 mAh/g, showing great advantage over the conventional Li-ion cathodes which typically have capacities of 150—180 mAh/g[5-10]. However, there are still problems need to be solved before these materials can be used in large scale for energy storage applications. One major problem is the so-called voltage fade phenomenon[11, 12]. Upon cycling, the average discharge voltage of these materials decreases continuously, resulting in the loss of energy and power densities after limited cycles[13, 14].

To understand the origin of voltage fade, various studies have been conducted by many groups worldwide and it is now generally concluded that voltage fade is associated with the layered-to-spinel phase transformation in LMR materials. Such phase transitions has been verified by microscopic[15-19], spectroscopic[18, 20, 21] and XRD[20, 21] experiments. Theoretical studies have indicated that Mn reduction (e.g., from $Mn^{4+}$ in the pristine material to $Mn^{3+}$ during cycling) is

particularly important for such layered-to-spinel phase transition[22]. As a result of such Mn reduction, oxygen release, which has been observed to occur at high voltage charge[23], is closely related to the phase transition and consequent voltage fade. Studies reported in the literature have confirmed this relationship and suggested approaches to mitigate voltage fade through manipulating the scale of oxygen release by substituting Mn with other transition metal elements[24, 25]. Although extensive studies have been reported on these two origins, the causes of the layered to spinel transition and oxygen loss have not been very well explored. Therefore, the better understanding of the factors which strongly influence the layered-to-spinel phase transformation and the oxygen release will help us to better understand these two issues in searching approaches to suppress the voltage fade.

It is well known that aside from structural and chemical properties, microstructure properties, such as crystallite size, grain boundaries, and other structural defects can also have great influence on the electrochemical performance of cathode materials[26-28]. However, their effects on voltage fade in LMR cathode materials are not clearly understood yet. There are scattered reports in the literature with observations of microstructure changes of LMR materials during electrochemical cycling. Ito *et al.*[29] found micro-cracks in highly charged (> 4.5 V) samples and suggested that these cracks could deteriorate the electrochemical performance in subsequent cycles. Zheng *et al.*[13] observed "sponge-like structure" and "fragmented pieces" on the surface of cathode after extended cycling. These works suggest that microstructure defects play important roles in the deterioration of electrochemical performance. These interesting results inspired our motivation of more detailed studies of the effects of microstructure defects on the layered-to-spinel phase transformation and oxygen release of LMR materials during cycling. To clearly link the effects of microstructure defects with the voltage fade, it would be quite helpful to find a set

of materials with same chemical stoichiometry and crystal structure, but different level of microstructure defects. It was found in this work that one type of LMR material—$Li_2Ru_{0.5}Mn_{0.5}O_3$[30, 31] can be used for this purpose through intentionally introducing microstructure defects by pre-lithiating the pristine material before the charge-discharge cycling. This material is chosen because it can accommodate large amount of extra lithium. This extra lithiation process generates large amount of microstructure defects and cause serious damage to the crystallinity of cathode material. When the extra lithium is extracted, the crystal structure and chemical composition pretty much change back to the pristine state but with preserved defects and severely damaged crystallinity, which can be studied for the effects on voltage fade in comparison with the same pristine material without prelithiation. It will be shown later in this paper that such loss of crystallinity and the other microstructure defects created by extra lithiation have significant influence on the voltage fade. Based on our x-ray diffraction (XRD), pair distribution function (PDF), x-ray absorption (XAS) and high-resolution transmission microscopy (HRTEM) studies, the correlations of voltage fade with poor crystallinity as well as with other microstructure defects are explored and the benefits of having high crystallinity and low level of microstructure defects are emphasized.

In the normal cycling, the LMR material $Li_2Ru_{0.5}Mn_{0.5}O_3$ is first charged (e.g., 4.6V) and then discharged (e.g., 2V). In order to insert extra lithium, a process called prelithiation was used by discharging the cell first. The effects of prelithiation on the voltage fade in subsequent cycling in comparison to the cell without prelithiation can be clearly seen in Figure 1. In Figure 1a, the cathode $Li_2Ru_{0.5}Mn_{0.5}O_3$ was first lithiated until the voltage decreased to 1V. A capacity of around 275 mAh/g was observed during this process, corresponding to about 1.2 extra Li inserted into the structure. We call this process ‘insertion process’ based on structural studies

which will be explained later. It can be seen that these amount of Li can be reversibly extracted as calculated from the capacity of next charge step. After the prelithiation, cathode material is normally cycled between 4.6 V and 2 V for 20 cycles and selected charge-discharge curves are plotted in Figure 1a. The same cathode material without prelithiation history was cycled in the same voltage range of 4.6 V and 2V as reference and the results are plotted in Figure 1b. Comparing the charge-discharge curves of these two cases, it is clear that the prelithiation process has a significant impact on the voltage fade in the subsequent cycling. Although prelithiation increases the discharge capacity, especially in the initial cycles (226 mAh/g Vs. 188 mAh/g for the second cycle), it considerably exacerbated voltage fade. Therefore, the detailed study of the structural changes caused by the prelithiation will provide important information for voltage fade suppression.

To study the structural changes during prelithiation process, *ex situ* XRD measurements were carried out on samples collected from the pristine state, the "OCV-1V" state (referring to the sample discharged to 1V) and the "OCV-1V-3V" state (referring to the sample first discharged to 1V and then charged to 3V) as shown in Figure 2. The XRD pattern of the pristine material features sharp Bragg peaks, indicating good crystallinity of the material. This is also confirmed by the Scanning Electron Microscope (SEM) image as shown in Figure S1. XRD pattern for the pristine state sample indicates a typical layered structure. In this structure, lithium and transition metal alternatively occupy the octahedral interstices layers in the framework of cubic-close-packed oxygen anions with the similar structure as $LiCoO_2$[7]. However, since $Li_2Ru_{0.5}Mn_{0.5}O_3$ is Li-rich (it can also be written as $Li(Li_{1/3}Ru_{1/3}Mn_{1/3})O_2$), some lithium ions occupy sites in the atomic layers which are supposed to be occupied by transition metal only in typical layer structured materials. These layers are referred as Li/Transition metal (Li/TM) layers[31]. Most of

the XRD peaks can be indexed by the $R\bar{3}m$ space group as in $LiCoO_2$ layer structured material. The additional diffuse and fairly asymmetric peaks between 19˚ and 25˚ are originated from the Li/Transition metal ordering in the Li/TM layer[32]. Going from pristine state to "OCV-1V-3V" state, it can be seen in Figure 2a, that peaks featuring the layered structure are still maintained, but they are considerably broadened. It is well documented that crystallite (or grain) size and stress are the two dominating factors contributing to XRD peak broadening. In this paper, we will focus on the grain size effects using pair distribution function (PDF) and high resolution transmission electron microscopy (TEM). In order to understand the micro structure defects created by prelithiation process, the structural changes during lithiation of $Li_2Ru_{0.5}Mn_{0.5}O_3$ is studied by analyzing the XRD pattern of "OCV-1V" state and the result is shown in the lower panel of Figure 2a. It can be seen that at "OCV-1V" state, the XRD results show Bragg reflections of two phases: the layered[30] (space group C2/m) phase and the so-called 1T phase (space group $P\bar{3}m1$). This is further supported by satisfactory Rietveld refinement carried out on the XRD pattern using these two phases as shown in Figure 2a. The so-called 1T phase was initially observed by Dahn *et al*.[33] when lithiating $LiNiO_2$ to yield $Li_2NiO_2$. The detailed structure was solved by Davidson *et al*. using neutron diffraction[34]. Later, this phase was also observed when lithiating $Li_{1+x}V_{1-x}O_2$[35], $Li_xNi_{0.5}Mn_{0.5}O_2$[36] and $Li(Ni_{0.5}Mn_{0.3}Co_{0.2})O_2$[37]. Transforming from the original layered phase to the 1T phase, the oxygen anion framework needs to be rearranged from cubic-close-packing to hexagonal-close-packing. Additionally, since the octahedral interstices can no longer provide enough sites for such large amount of lithium, lithium ions originally occupying octahedral sites need to move to tetrahedral sites adjacent to the original lithium layer, together with the extra lithium ions introduced. Therefore, in this 1T phase, transition metal ions occupy octahedral sites and lithium ions occupy tetrahedral sites as

illustrated in Figure 2b. Derived by Rietveld refinement, the unit cells dimensions of these two phases are marked in Figure 2b. It can be seen that considerable volume expansion is involved when layered structure transforms to 1T. Firstly, the bond distance of transition metal—transitional metal is increased from 2.89 Å to 3.10 Å as a result of transition metal reduction; secondly, the distance between two transition metal layers is also increased from 4.80 Å to 5.10 Å to accommodate the large amount of lithium ions. These two increased distances add up to a 22% volume expansion (from 104.2 $Å^3$ in layered to 127.3 $Å^3$ in 1T). It is believed that this large volume expansion creates significant strain inside the particle and consequently leads to the creation of micro structural defects and new grain boundaries in the material. Due to some residues of 1T phase, there are some low intensity peaks located at the left side of the main phase peaks (1T phase has larger lattice parameters than the layered phase of the pristine material). Visually, this appears as the main phase peaks broadened more to lower angles. As we can see from Figure 1, that the discharge capacity (~275 mAh/g) of prelithiated $Li_2Ru_{0.5}Mn_{0.5}O_3$ is higher than the subsequent charge capacity (~210 mAh/g) when charged back to 3V, meaning ~65 mAh/g of Li remains in the structure after re-charging. The percentage of 1T phase in the "OCV-1V-3V" sample is estimated about 20%. However, the more important issue is the amount of 1T residues in the prelithiated sample at OCV—1V—3V-4.6V-2Vstate. Based on the electrochemical results in Figure 1, most of the residues of 1T phase in the "OCV-1V-3V" sample should be consumed during the high voltage charging from 3V to 4.6V and not much new 1T phase can be reformed during discharge from 4.6V to 2V. Therefore, the amount of 1T phase for the prelithiated sample in the 2V-4.6V-2V subsequent cycling should be quite low. The residues of 1T phase in the prelithiated sample is rather low at OCV—1V—3V-4.6V-2Vstate, and they are inactive in the 2V to 4.6V cycling range (the formation of 1T phase is as low as

1.3V), and their effects are mostly taken place through forming the interphases as one type of microstructural defects. Therefore, their contribution to the voltage fading is limited. As shown in the XRD pattern comparison between pristine state and "OCV-1V-3V" state earlier in this paper, when extra lithium is extracted out, although the crystal structure mostly changes back to the original layered phase, it suffers from the poorer crystallinity caused by the prelithiation process. This is further supported by the XAS results plotted in Figure S2, showing XAS spectra for the pristine sample and for the OCV—1V—3V one are fairly similar. Both Mn K-edge and Ru K-edge XANES spectra shift to lower energies during discharging to 1V and shifts back to almost the pristine state when charged to 3V. At the OCV—1V—3V state, both Mn K-edge and Ru K-edge spectra are at little bit lower energy than the pristine one, suggesting they're still slightly reduced than the pristine state. This is in good agreement with the conclusion that some 1T phase remains in the OCV—1V—3V sample. The EXAFS and Fourier Transformed spectra in Figure S2b and Figure S2c show that the local environments of Mn and Ru are basically the same in the pristine and OCV—1V—3V samples. On the other hand, there is an obvious amplitude reduction from the pristine to the OCV—1V—3V sample for both EXAFS and Fourier Transformed spectra. This is attributed to the decreased grain size, reduced coordination number and increased structural disorder, consistent with what directly observed in STEM and deduced from PDF data.

In order to study the effects of prelithiation on long and short range ordering, the pair distribution function (PDF) measurements were performed and the results are shown in Figure 3. Unlike the XRD analysis which provides three dimensional information of electron density through Fourier transformation of Bragg scattering (requires long range ordering of the sample) collected in the reciprocal space, PDF provides the information of atomic pair distribution (distance between two

atoms and the coordination number) through Fourier transformation of total scattering (both Bragg scattering that originates from long range periodicity and diffuse scattering that originates from local distortion, and therefore, no long range ordering is required)[38, 39]. PDF as the Fourier transformed form of total scattering data can provide information both in the long range and in the short range. Therefore, PDF has unique advantage in analyzing materials with limited structural coherence length. In Figure 3a, a simplified way to interpret basic results of PDF is illustrated, showing that PDF peaks correspond to characteristic bond distances in the material while the amplitude of the peak is relating to the coordination number. Take the conventional layered material as an example ($LiNiO_2$), the first peak (in red) is mainly from transition metal—oxygen bond and the peak position corresponds to the transition metal—oxygen bond length. Lithium-oxygen bond also contributes to the first peak but the contribution is negligible considering the small scattering power of lithium. Likewise, the second peak (in blue) is mainly from transition metal—transition metal bond. The PDF data for pristine state and "OCV-1V-3V" state are shown in Figure 3b, providing structural information in the scale of around 50 Å. It can be seen that in the short range region (Figure 3c) which covers from 1.6 Å to around 20 Å, the two data sets are almost identical. This indicates that at the scale of a unit cell dimension, the pristine state and "OCV-1V-3V" state have very similar atomic arrangements, suggesting their crystal structure are basically the same. However, when it comes to long range data sets as shown in Figure 3d, there is obvious difference between these two states. For the pristine state, there are still well-defined structural features at R value as high as 50 Å. However, for "OCV-1V-3V" state, these structural features are gradually lost when R is greater than 35 Å, indicating that the coherently scattering domain is on the scale of several nanometers[40, 41]. This is consistent

with the conclusion we drew from XRD analysis discussed previously and microscopic studies to be explained below.

Microstructure changes and nano-sized microstructural defects created by prelithiation process can be directly observed by comparing the Z-contrast annular dark-field scanning transmission electron microscopic (ADF-STEM) images taken on pristine and prelithiated samples. Figure 4a (left panel) shows the atomic-resolution ADF-STEM image of the pristine material, indicating good crystallinity with typical features of the layered structure. After prelithiation, the material (right panel, Figure 4a) shows great loss of the crystallinity, forming domains that orient differently from each other with large amount of additional grain boundaries created. It can be seen that these domains are at the scale of several nanometers, confirming previous analysis of XRD and PDF results. The process is illustrated in Figure 4b.

Previous discussions suggest that the prelithiation process reduced the coherent scattering length of the cathode material crystal from sub-micro size to a few nanometer size by creating many nano-sized domains within the original crystal grain. Apparently, such loss of crystallinity has significant impact on voltage fade. As shown in Figure 1a, at the $20^{th}$ cycle, more than 2/3 of the discharge capacity for the prelithiated sample is in the low voltage region (< 3V). In contrast, the discharge capacity for the sample without pre-lithiation is still mainly in the high voltage region (> 3V). This implies that in the prelithiated sample, an increased portion of the reduction reaction during discharge is contributed by transition metal cations with lower valence state than the sample without prelithiation. In other words, the prelithiated sample experiences more reduction. To confirm this assumption, *ex situ* XAS experiments were carried out from samples after 20 cycles and the results are shown in Figure 5a. The sample collected from the cell that had been cycled 20 times with initial prelithiation is referred as “OCV-1V-(4.6V-2V)20Cy” and the one

collected from the cell that had been cycled 20 times without prelithiation is referred as "OCV-(4.6V-2V)20Cy". Both "OCV-1V-(4.6V-2V)20Cy" and "OCV-(4.6V-2V)20Cy" samples were measured at 2V discharged state after 20 cycles. Although discharged to the same voltage may not guarantee the two samples are at exactly same electrochemical state (or exactly same Li content), but they should not be too far apart. Figure 5a indicates that transition metal cations in both "OCV-1V-(4.6V-2V)20Cy" sample and "OCV-(4.6V-2V)20Cy" sample experience reduction during cycling. This is true both for Mn and Ru as seen from the edges shifting to the lower energy in both Mn K-edge spectra and Ru K-edge spectra. More importantly, for the Mn K-edge, while the "OCV-1V-(4.6V-2V)20Cy" spectrum is already close to the $Mn_2O_3$ reference, the "OCV-(4.6V-2V)20Cy" spectrum still lies close to the $MnO_2$ reference. This suggests that Mn is mostly trivalent in "OCV-1V-(4.6V-2V)20Cy" state and mostly tetravalent in "OCV-(4.6V-2V)20Cy" state. Therefore, it is expected that the discharge capacity for prelithiated sample is mostly contributed by the $Mn^{3+}/Mn^{4+}$ redox couple at the $20^{th}$ cycle and this redox couple leads to lower discharge voltage. In contrast, the redox-active cations in normally cycled sample "OCV-(4.6V-2V)20Cy" are still mostly $Ru^{4+}/Ru^{5+}$ as suggested by Sathiya *et al*[30].

Such extra reduction of transition metal in "OCV-1V-(4.6V-2V)20Cy" sample suggests that additional oxygen was released from this sample during cycling. Oxygen release has previously been observed in Li-rich cathode materials when they are charged to high voltages[23, 31, 42] and is also expected to occur in the studied material $Li_2Ru_{0.5}Mn_{0.5}O_3$ as well. Interestingly, "OCV-1V-(4.6V-2V)20Cy" sample apparently released much more oxygen than the "OCV-(4.6V-2V)20Cy" one. This difference can be attributed to the loss of crystallinity caused by prelithiation. First, the micro structural defects, such as grain boundaries, are favorable for oxygen vacancy diffusion that leads to additional oxygen release. Secondly, possible higher surface area might be resulted

from the prelithiation, which is also favorable for oxygen release. As suggested by Delmas *et al*., oxygen is mainly released from the surface rather than from the bulk[43, 44]. Such extra oxygen release in "OCV-1V-(4.6V-2V)20Cy" sample might be responsible for the followings:

(1) It directly leads to transition metal reduction and gets lower valence transition metal (e.g., $Mn^{3+}$) to be more and more involved in the redox process. This is manifested as decrease in discharge voltage or voltage fade.

(2) Oxygen release is not only exacerbated by the micro structural defects, but also promotes the formation of defects which in turn leads to further oxygen release. In other words, oxygen release and defect formation form a positive feedback loop. Evidence comes from ex situ XRD studies shown in Figure 5b. The figure is separated by a dash line in the middle. The upper part corresponds to the prelithiated case and the lower one to the normally cycled case. Similar to the notation used before, "OCV-1V-(4.6V-2V)8Cy" and "OCV-(4.6V-2V)8Cy" refer to the $8^{th}$ cycle samples from prelithiated and normally cycled cells respectively. Compared with the normally cycled case, samples in the prelithiated case show much greater peak broadening and this broadening effect increases as the cycle number increases. This indicates that the loss of crystallinity is not just a one-time-event that only happens in the first cycle, but can be promoted by oxygen release and deteriorate in the following cycles. In turn, this facilitates further oxygen release.

(3) Oxygen release and microstructural defects also accelerates spinel formation. This can be seen from Figure 5c which gives the evolution of lattice parameter *c* to lattice parameter *a* ratio during cycling. The lattice parameter *c* and *a* are obtained from fitting the XRD patterns using $R\bar{3}m$ symmetry instead of the more complicated *C2/m* symmetry to simplify the discussion. Crystallographic analysis indicates when $c/a = 2\sqrt{6}$, the unit cell of the layered structure can be

defined as cubic simply by changing the basis[45]. In other words, when $c/a = 2\sqrt{6}$, the layered structure totally changes into the spinel. In Figure 5c, c/a ratio of the "OCV-1V-(4.6V-2V)20Cy" sample is much closer to this value than the "OCV-(4.6V-2V)20Cy" one, indicating much more spinel is formed inside the sample of "OCV-1V-(4.6V-2V)20Cy". Such accelerated spinel phase formation can also be evidenced by the merging of (108) and (110) peaks (indexed using the $R\bar{3}m$ space group for easy comparison) for OCV-1V-(4.6V-2V)8Cy" and OCV-1V-(4.6V-2V)20Cy" samples in Figure 5b. In contrast, the (108) and (110) peaks are still well separated for both "OCV-(4.6V-2V)"and "OCV-(4.6V-2V)20Cy" samples. As discussed previously, there is much more oxygen loss in "OCV-1V-(4.6V-2V)20Cy" than in "OCV-(4.6V-2V)20Cy". How spinel formation is promoted by oxygen loss can be understood by considering the dumbbell formation. As pointed out by Ceder *et al.*[22, 46], the critical kinetic step in the layered-to-spinel transformation is the formation of dumbbell defect[47] which features transition metal occupying tetrahedral site. Specifically, the tendency of such tetrahedral occupation is strongly dependent on the electronic structure of the cation[48, 49]. $Mn^{3+}$ has been proved to be very prone to tetrahedral site occupation through the disproportionation reaction $2Mn^{3+} \rightarrow Mn^{2+} + Mn^{4+}$. In "OCV-1V-(4.6V-2V)20Cy" sample, there are higher concentration of $Mn^{3+}$ resulted from more oxygen loss. These $Mn^{3+}$ ions facilitate dumbbell defects formation and promote the layered-to-spinel transformation.

The effects of micro structural defects on the voltage fade is illustrated schematically in Figure 6. By clarifying such mechanism, valuable guidance can be provided for finding the paths to suppress voltage fade in LMR materials. For some Li-ion battery cathode materials, small particle size is favored because the reduced lithium ion transport length can enhance the electrochemical reaction and high rate capability. A classic example is $LiFePO_4$, which has

dramatic improvement in electrochemical performance when the crystallite size is small enough. Recent studies on $Li(Ni_{0.5}Mn_{0.3}Co_{0.2})O_2$[37] indicate that small particle size may also be beneficial for conventional layered materials. However, for LMR materials with the problem of oxygen loss at high voltage, the situation is quite different. In this paper, using XRD, PDF, and TEM, the effects of accelerating oxygen loss by micro structural defects including grain boundaries are clearly demonstrated. Such effects are very likely to be caused by the increased surface area of materials with smaller particle size as well considering the sluggish kinetic nature of LMR materials[50]. Therefore, in order to suppress the voltage fade in LMR materials, it is necessary to (1) minimize the level of microstructural defects (e.g., increasing the crystallite or grain size to reduce the grain boundaries). (2) modify the surface of LMR materials with protection layer. These approaches have also been proposed by other researchers in recent studies[43, 44, 51]. There are recent examples of improving electrochemical performance[52-54], especially suppressing voltage fade[54], by applying surface modification using $Al_2O_3$[55], $AlF_3$[56] and even lithium-conducting materials like LiPON[52] and $LiFePO_4$[54]. The results of structural studies reported in this paper provide important scientific base for using surface protection approaches such as coating to suppress the voltage fade in LMR materials.

It should be noted that in practical operations, cathode material is rarely discharged to a voltage as low as 1V which is used in this study. As a result, prelithiation is unlikely to happen under normal conditions. However, due to the inhomogeneity of electrochemical reaction, it is reasonable to expect some areas are more deeply lithiated than the nominal average level, especially when high rate discharging at low temperatures. These areas may be regarded as "locally prelithiated". As demonstrated in this work, such prelithiation is harmful for the electrochemical performance of LMR materials, inducing significant microstructure changes,

which ultimately lead to accelerated voltage fade. This suggests that not only the charge cut-off voltage is closely related to the voltage fade (which has been shown by several studies[1, 2]), the discharge cut-off voltage has great influence as well. Increasing the discharge cut-off voltage can have positive effect on reducing the voltage fade through minimizing the possibility local prelithiation, which can be clearly seen in Figure S3, showing that increasing the discharge cut-off voltage does mitigate the voltage fade.

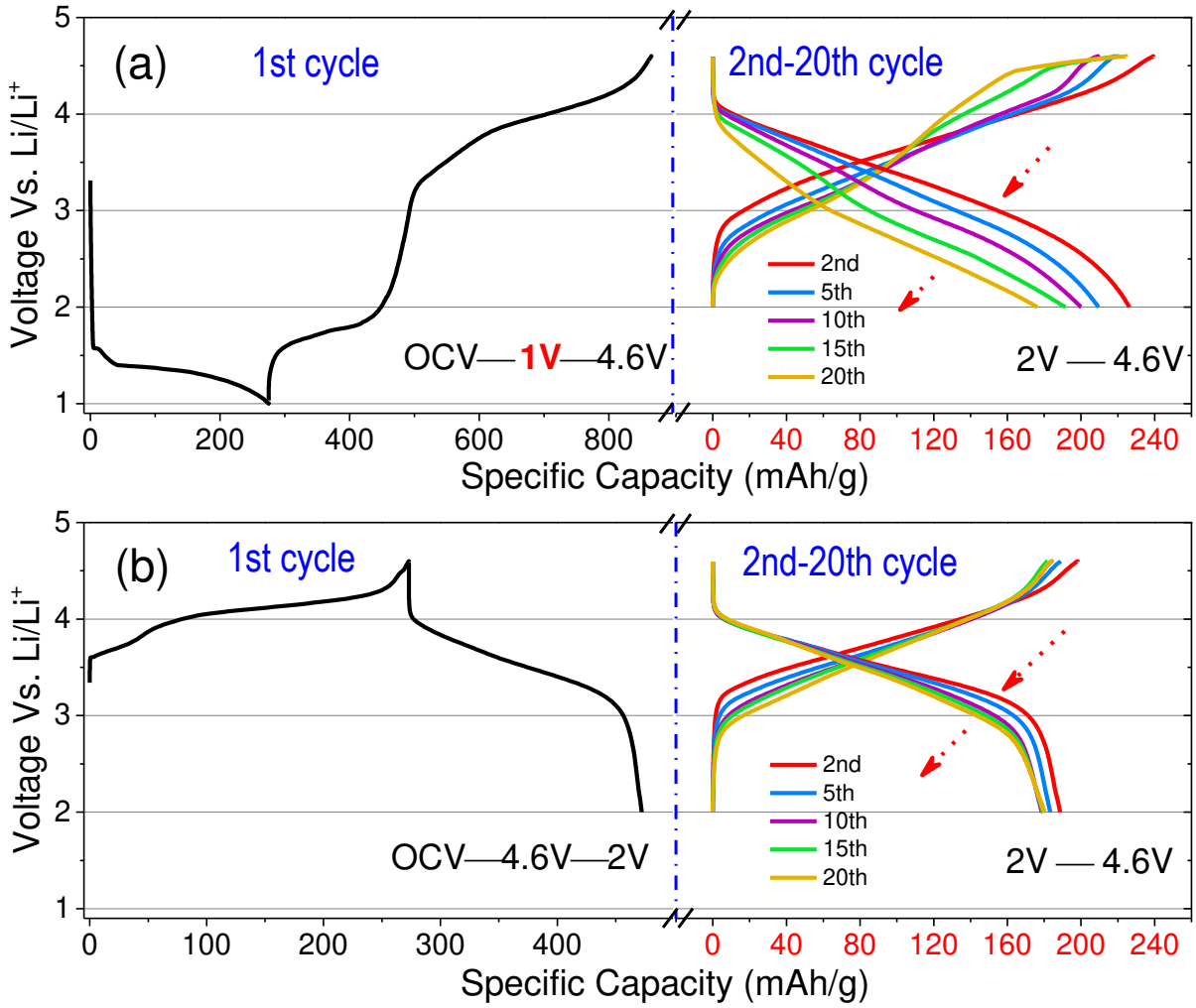


Figure 1 Electrochemical performances of (a) prelithiated $Li_2Ru_{0.5}Mn_{0.5}O_3$which is first discharged to 1 V and then charged to 4.6 V, followed by cycling between 2V and 4.6 V; (b) normally cycled $Li_2Ru_{0.5}Mn_{0.5}O_3$ which is directly cycled between 2 V and 4.6 V without discharging first. The current used is C/8, corresponding to 0.07 mA/cm$^2$ in all cases.

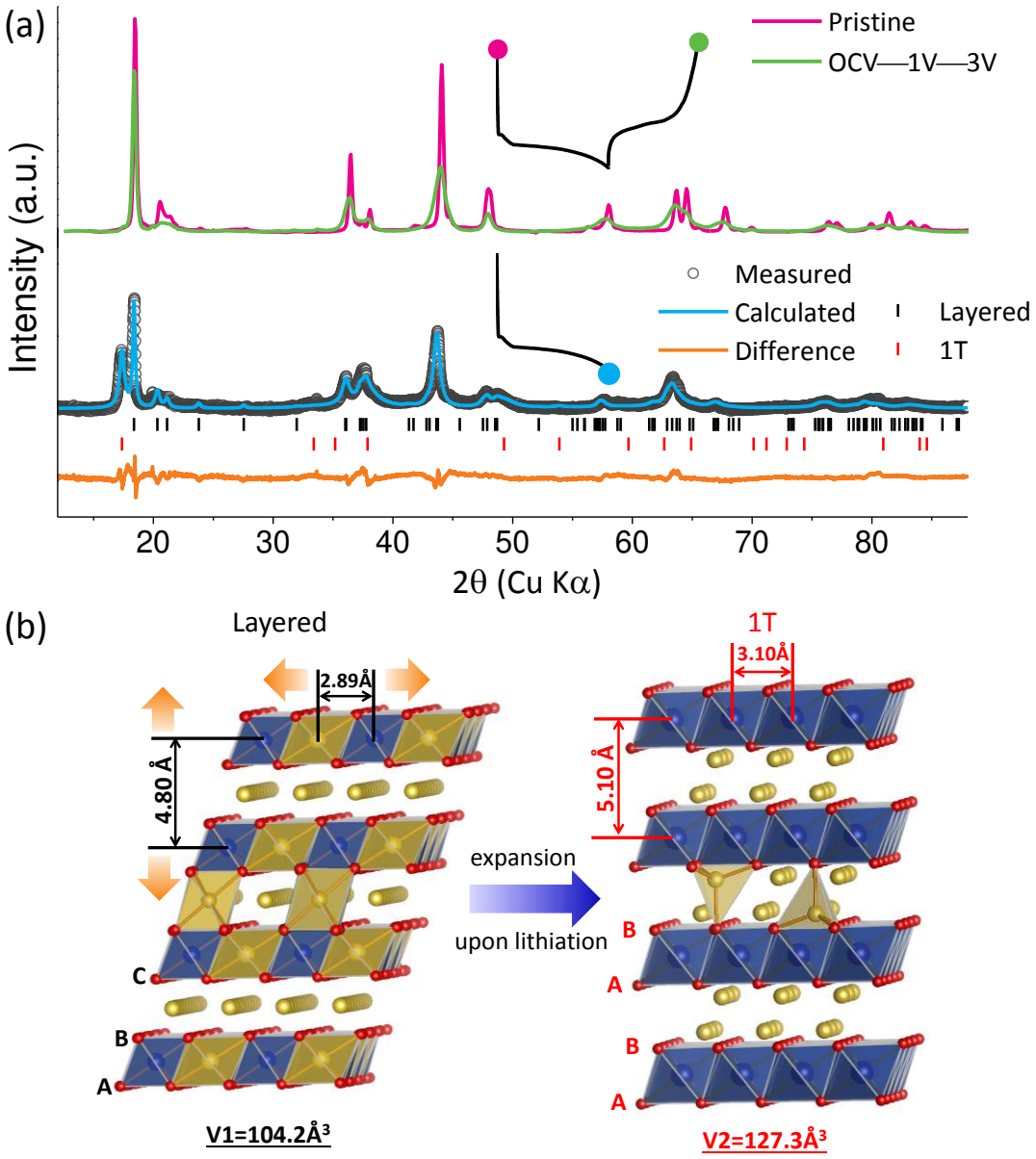


Figure 2 (a) *Ex situ* XRD studies of $Li_2Ru_{0.5}Mn_{0.5}O_3$ during prelithiation process. The upper panel shows XRD patterns of the pristine sample and the sample that is first discharged to 1 V and then charged to 3 V (OCV—1V—3V). The lower panel shows results from Rietveld refinement of the sample discharged to 1 V (OCV—1V), with experimental data shown in dotted circles, fitted data shown in blue, and difference shown in orange. (b) Structure illustrations of layered phase and 1T phase, showing volume expansion during phase transition.

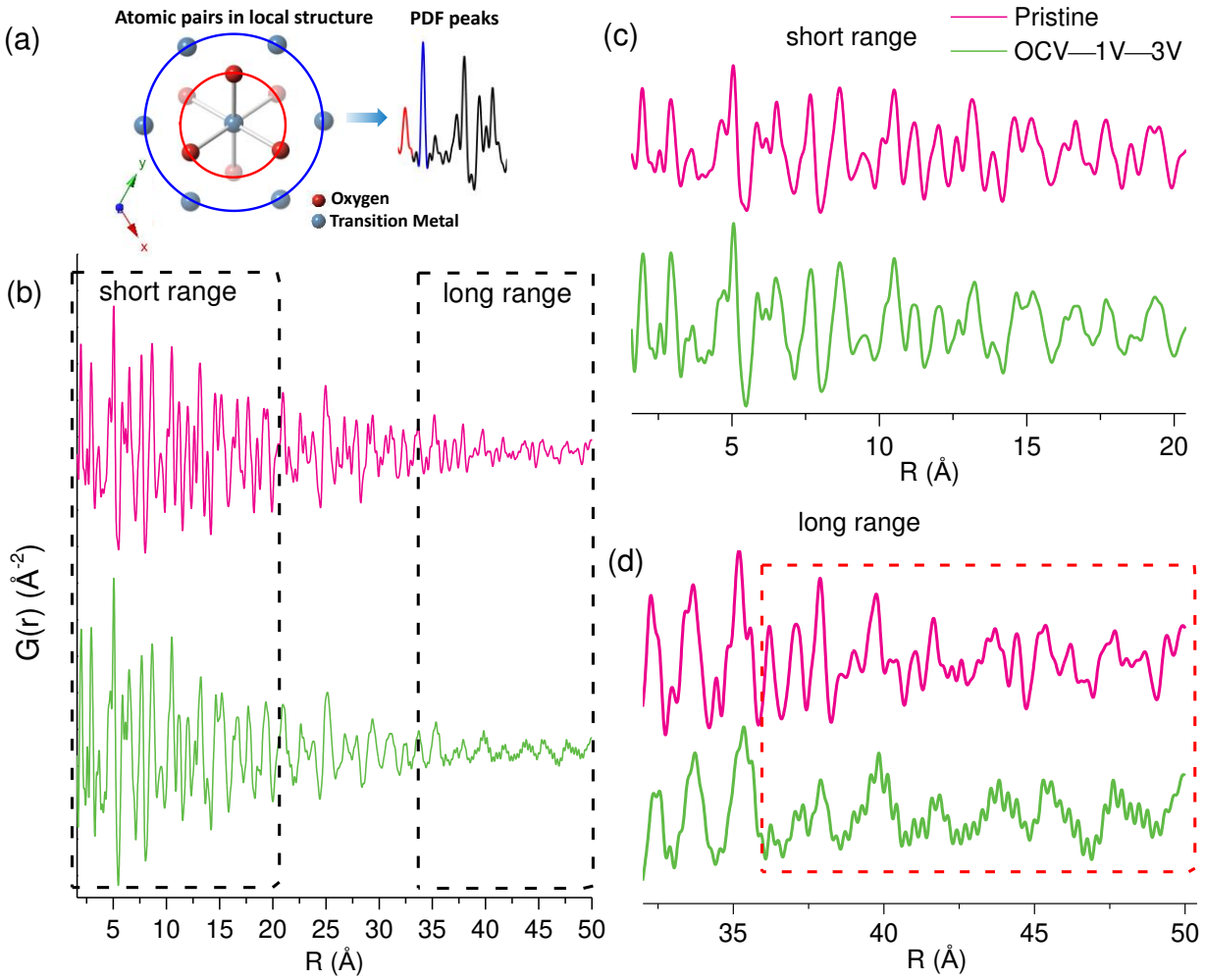


Figure 3 (a) Illustration of PDF showing that peaks correspond to characteristic bond lengths. (b) *Ex situ* PDF data of pristine sample and "OCV—1V—3V" sample (c) zoomed in data on the short range region of ex situ PDF data and (d) zoomed in data on the long range region of *ex situ* PDF data.

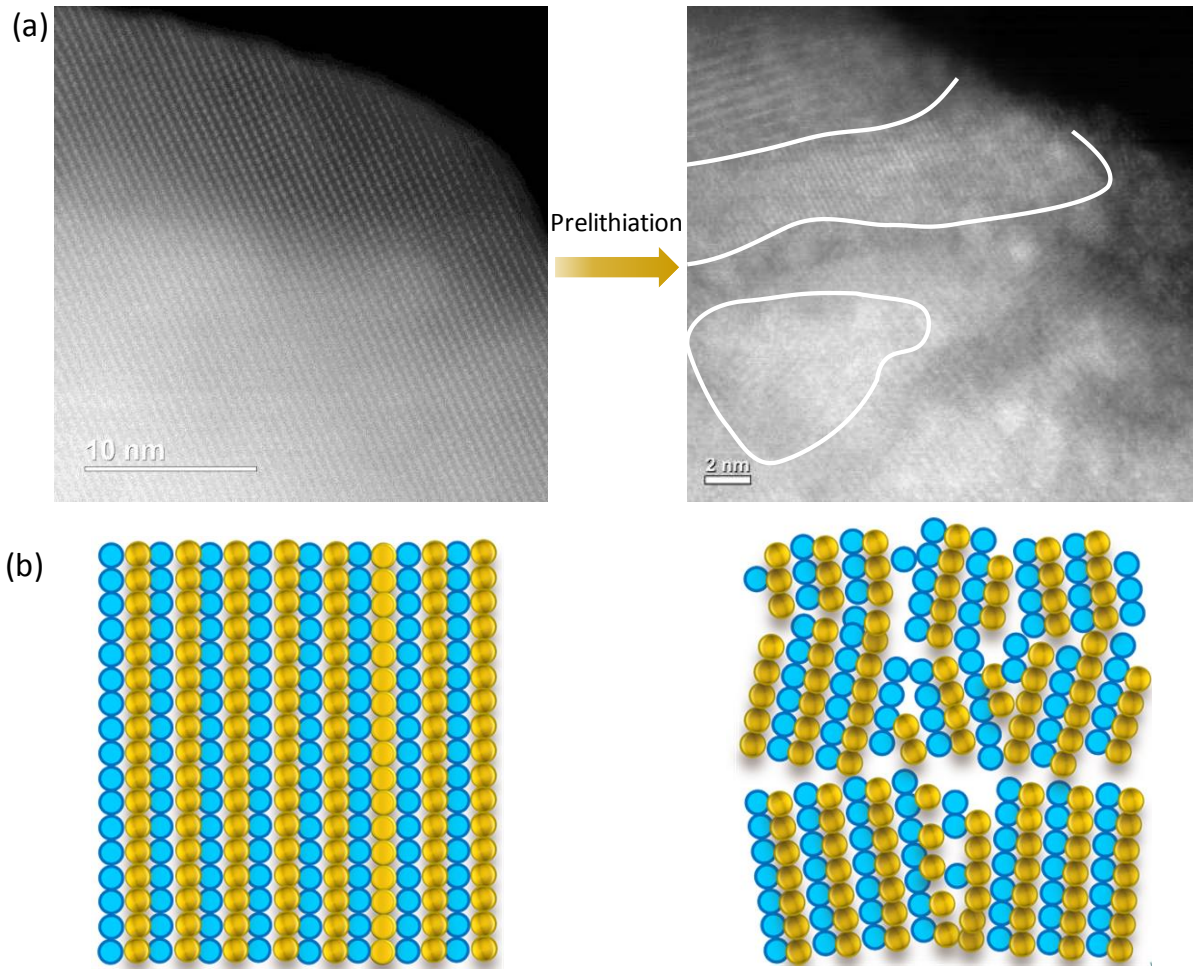


Figure 4 (a) Z-contrast scanning transmission electron microscopic (STEM) images of pristine sample and "OCV—1V—3V" sample. In the "OCV—1V—3V" sample, a few selected domains are circled out by the white lines. (b) Illustration of the microstructure change brought by prelithiation process.

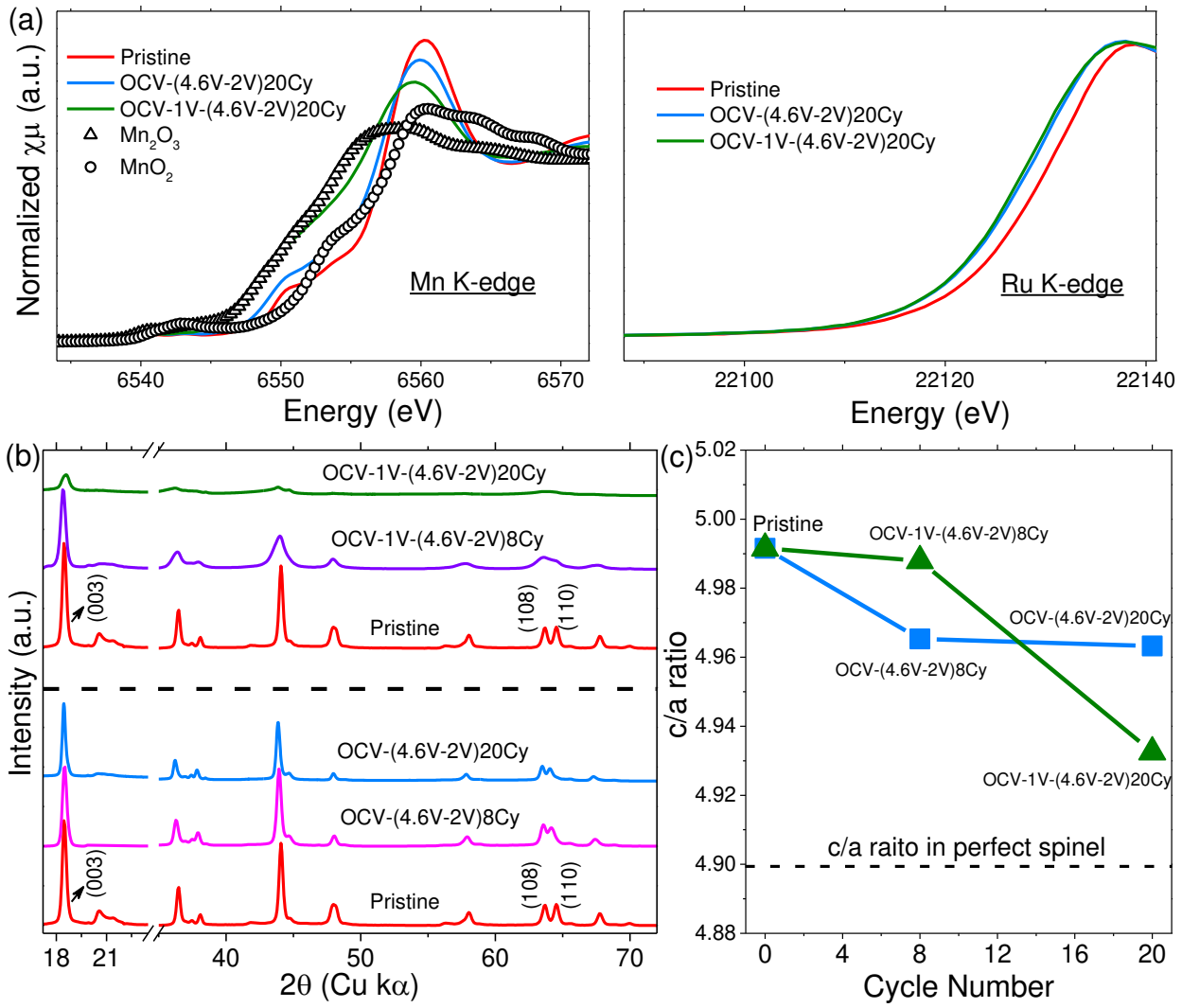


Figure 5 (a) *ex situ* Mn K-edge and Ru K-edge XAS data of pristine sample, sample normally cycled 20 times and sample cycled 20 times but first prelithiated, with references of $Mn_2O_3$ and $MnO_2$ shown. (b) *Ex situ* XRD patterns of two cases (with (003), (108) and (110) peaks indexed according to the space group $R\bar{3}m$): pristine sample, cycled 8 times and cycled 20 times for the normally cycled case (the part below the dash line); pristine sample, cycled 8 times and cycled 20 times for the prelithiated case (the part above the dash line). (c) The ratio between lattice parameter *c* and lattice parameter *a* as a function of cycle numbers. The dash line shows the *c*/*a* ratio in perfect spinel.

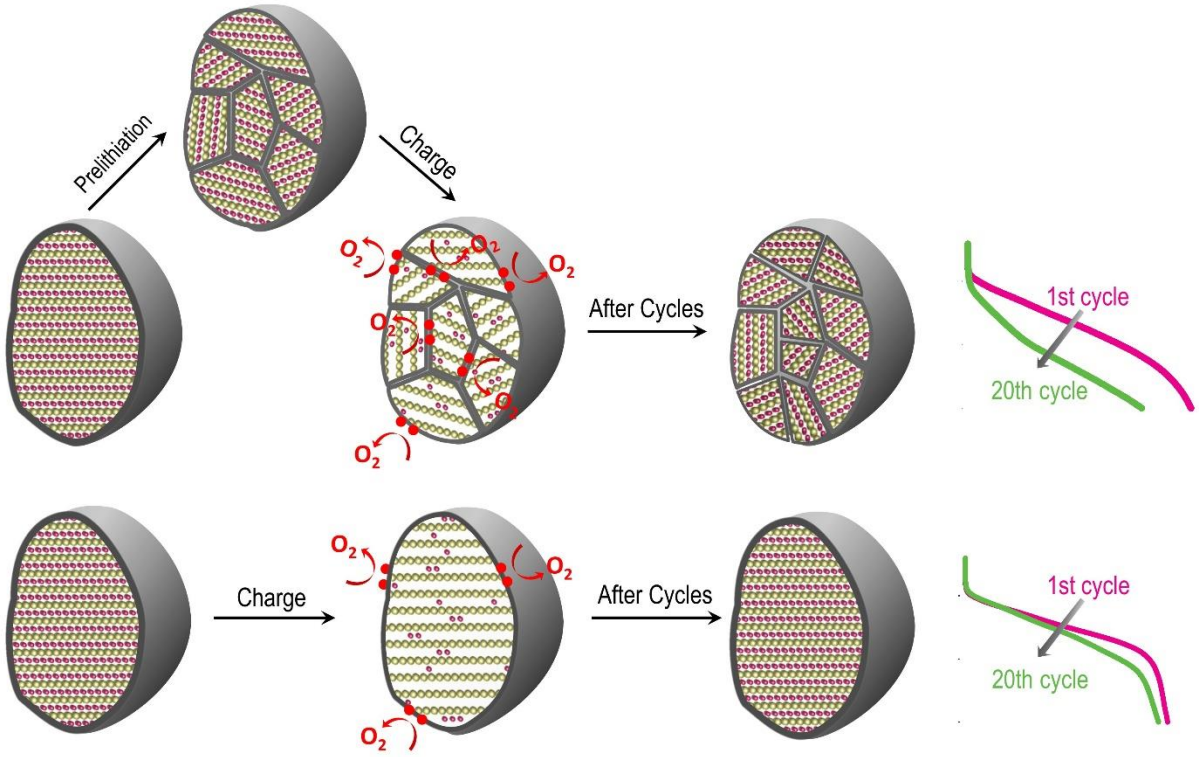


Figure 6 Illustration of prelithiation-induced smaller crystallite size and its effect on voltage fade in $Li_2Ru_{0.5}Mn_{0.5}O_3$.

**Supporting Information**

Further details on materials synthesis and characterization methods, SEM image of pristine material, evaluation of 1T phase fraction, XAS data of ex situ samples and the effect of cut-off discharge voltage on voltage fade. This material is available free of charge via the Internet at http://pubs.acs.org.

**Corresponding Authors**

*E-mail: xyang@bnl.gov (X.Q.Y.)

*E-mail: xyu@iphy.ac.cn (X.Y.)

*E-mail: hli@iphy.ac.cn (H.L.)

**Author Contributions**

E.H. and X.Y. designed the project. Y.L. synthesized the material. E.H. performed electrochemical measurements. H.L.X. and L.H. performed STEM measurements. E.H., J.L., X.Y. and J.B. performed PDF measurements. E.H. and S.B. performed XAS measurements. E.H., H.L.X., J.L., X.Y., H.L. and X.Q.Y. contributed to data interpretation. E.H., X.Y., and X.Q.Y. wrote the manuscript. X.Q.Y. coordinated the manuscript submission. All authors participated in the discussions of the results as well as preparing the paper.

**Notes**

The authors declare no competing financial interest. E. H. and Y.L. contributed equally to this work.

**Acknowledgement**

The authors are grateful to the inspiring scientific discussion with Dr. Eric Dooryhee from XPD beamline (28ID) at NSLS-II. The work at Brookhaven National Laboratory was supported by the U.S. Department of Energy, the Assistant Secretary for Energy Efficiency and Renewable Energy, Office of Vehicle Technologies under Contract No. DE-SC0012704. Use of the beamline (28ID) at National Synchrotron Light Source II (NSLS-II) and STEM at Center for Functional Nanomaterials of Brookhaven National Laboratory were supported by the U.S. Department of Energy, Office of Science, Office of Basic Energy Sciences, under Contracts No. DE-SC0012704. Y. Lyu is supported by the Shanghai Municipal Science and Technology Commission (No. 14DZ2261200). H. Li is supported by National Science Foundation of China (51325206, 51421002), “Strategic Priority Research Program” of the Chinese Academy of

Sciences (XDA09010000) and National project 973 (2012CB932900). We acknowledge technical support from the scientists at beamline 12-BM-B and 17-BM-B of APS (ANL), supported by the U.S. DOE under Contract No. DE-AC02-06CH11357. Part of this research was conducted at the BL2-2 of Stanford Synchrotron Radiation Lightsource. Use of the Stanford Synchrotron Radiation Lightsource, SLAC National Accelerator Laboratory, is supported by the U.S. Department of Energy, Office of Science, Office of Basic Energy Sciences under Contract No. DE-AC02-76SF00515.

**References**

1. Lu, Z.; Dahn, J. R. *J. Electrochem. Soc.* **2002,** *149*, A815-A822.
2. Thackeray, M. M.; Kang, S.-H.; Johnson, C. S.; Vaughey, J. T.; Benedek, R.; Hackney, S. *J. Mater. Chem.* **2007,** *17*, 3112-3125.
3. Lee, J.; Urban, A.; Li, X.; Su, D.; Hautier, G.; Ceder, G. *Science* **2014,** *343*, 519-522.
4. McCalla, E.; Abakumov, A. M.; Saubanere, M.; Foix, D.; Berg, E. J.; Rousse, G.; Doublet, M. L.; Gonbeau, D.; Novak, P.; Van Tendeloo, G.; Dominko, R.; Tarascon, J. M. *Science* **2015,** *350*, 1516-1521.
5. Herle, P. S.; Ellis, B.; Coombs, N.; Nazar, L. F. *Nat. Mater.* **2004,** *3*, 147-52.
6. Tarascon, J. M.; Armand, M. *Nature* **2001,** *414*, 359-67.
7. Mizushima, K.; Jones, P.; Wiseman, P.; Goodenough, J. B. *Mater. Res. Bull.* **1980,** *15*, 783-789.
8. Padhi, A. K.; Nanjundaswamy, K.; Goodenough, J. *J. Electrochem. Soc.* **1997,** *144*, 1188-1194.
9. Thackeray, M.; David, W.; Bruce, P.; Goodenough, J. *Mater. Res. Bull.* **1983,** *18*, 461-472.
10. Thackeray, M.; Johnson, P.; De Picciotto, L.; Bruce, P.; Goodenough, J. *Mater. Res. Bull.* **1984,** *19*, 179-187.
11. Dogan, F.; Long, B. R.; Croy, J. R.; Gallagher, K. G.; Iddir, H.; Russell, J. T.; Balasubramanian, M.; Key, B. *J. Am. Chem. Soc.* **2015,** *137*, 2328-2335.
12. Sathiya, M.; Abakumov, A. M.; Foix, D.; Rousse, G.; Ramesha, K.; Saubanere, M.; Doublet, M. L.; Vezin, H.; Laisa, C. P.; Prakash, A. S.; Gonbeau, D.; VanTendeloo, G.; Tarascon, J. M. *Nat. Mater.* **2015,** *14*, 230-8.
13. Zheng, J.; Gu, M.; Xiao, J.; Zuo, P.; Wang, C.; Zhang, J. G. *Nano Lett.* **2013,** *13*, 3824-30.
14. Zheng, J.; Gu, M.; Genc, A.; Xiao, J.; Xu, P.; Chen, X.; Zhu, Z.; Zhao, W.; Pullan, L.; Wang, C.; Zhang, J. G. *Nano Lett.* **2014,** *14*, 2628-35.
15. Gu, M.; Belharouak, I.; Zheng, J. M.; Wu, H. M.; Xiao, J.; Genc, A.; Amine, K.; Thevuthasan, S.; Baer, D. R.; Zhang, J. G.; Browning, N. D.; Liu, J.; Wang, C. M. *Acs Nano* **2013,** *7*, 760-767.
16. Xu, B.; Fell, C. R.; Chi, M. F.; Meng, Y. S. *Energy Environ. Sci.* **2011,** *4*, 2223-2233.
17. Oh, P.; Ko, M.; Myeong, S.; Kim, Y.; Cho, J. *Adv. Energy Mater.* **2014,** *4*.

18. Nayak, P. K.; Grinblat, J.; Levi, M.; Aurbach, D. *Electrochim. Acta* **2014,** *137*, 546-556.
19. Yan, P. F.; Nie, A. M.; Zheng, J. M.; Zhou, Y. G.; Lu, D. P.; Zhang, X. F.; Xu, R.; Belharouak, I.; Zu, X. T.; Xiao, J.; Amine, K.; Liu, J.; Gao, F.; Shahbazian-Yassar, R.; Zhang, J. G.; Wang, C. M. *Nano Lett.* **2015,** *15*, 514-522.
20. Hong, J.; Seo, D. H.; Kim, S. W.; Gwon, H.; Oh, S. T.; Kang, K. *J. Mater. Chem.* **2010,** *20*, 10179-10186.
21. Amalraj, S. F.; Burlaka, L.; Julien, C. M.; Mauger, A.; Kovacheva, D.; Talianker, M.; Markovsky, B.; Aurbach, D. *Electrochim. Acta* **2014,** *123*, 395-404.
22. Reed, J.; Ceder, G. *Chem. Rev.* **2004,** *104*, 4513-4533.
23. Armstrong, A. R.; Holzapfel, M.; Novak, P.; Johnson, C. S.; Kang, S. H.; Thackeray, M. M.; Bruce, P. G. *J. Am. Chem. Soc.* **2006,** *128*, 8694-8698.
24. Deng, Z. Q.; Manthiram, A. *J Phys Chem C* **2011,** *115*, 7097-7103.
25. Lee, E. S.; Manthiram, A. *J. Mater. Chem. A* **2014,** *2*, 3932-3939.
26. Chen, L.; Su, Y. F.; Chen, S.; Li, N.; Bao, L. Y.; Li, W. K.; Wang, Z.; Wang, M.; Wu, F. *Adv. Mater.* **2014,** *26*, 6756-6760.
27. Liu, W.; Oh, P.; Liu, X.; Myeong, S.; Cho, W.; Cho, J. *Adv. Energy Mater.* **2015,** *5*.
28. Dixit, H.; Zhou, W.; Idrobo, J. C.; Nanda, J.; Cooper, V. R. *Acs Nano* **2014,** *8*, 12710-12716.
29. Ito, A.; Li, D.; Sato, Y.; Arao, M.; Watanabe, M.; Hatano, M.; Horie, H.; Ohsawa, Y. *J. Power Sources* **2010,** *195*, 567-573.
30. Sathiya, M.; Ramesha, K.; Rousse, G.; Foix, D.; Gonbeau, D.; Prakash, A.; Doublet, M.; Hemalatha, K.; Tarascon, J.-M. *Chem. Mater.* **2013,** *25*, 1121-1131.
31. Sathiya, M.; Rousse, G.; Ramesha, K.; Laisa, C. P.; Vezin, H.; Sougrati, M. T.; Doublet, M. L.; Foix, D.; Gonbeau, D.; Walker, W.; Prakash, A. S.; Ben Hassine, M.; Dupont, L.; Tarascon, J. M. *Nat. Mater.* **2013,** *12*, 827-35.
32. Bréger, J.; Jiang, M.; Dupré, N.; Meng, Y. S.; Shao-Horn, Y.; Ceder, G.; Grey, C. P. *J. Solid State Chem.* **2005,** *178*, 2575-2585.
33. Dahn, J.; von Sacken, U.; Michal, C. *Solid State Ionics* **1990,** *44*, 87-97.
34. Davidson, I.; Greedan, J.; Von Sacken, U.; Michal, C.; Dahn, J. *Solid State Ionics* **1991,** *46*, 243-247.
35. Armstrong, A. R.; Lyness, C.; Panchmatia, P. M.; Islam, M. S.; Bruce, P. G. *Nat. Mater.* **2011,** *10*, 223-229.
36. Johnson, C. S.; Kim, J.-S.; Kropf, A. J.; Kahaian, A. J.; Vaughey, J. T.; Fransson, L. M.; Edström, K.; Thackeray, M. M. *Chem. Mater.* **2003,** *15*, 2313-2322.
37. Wu, Z.; Ji, S.; Zheng, J.; Hu, Z.; Xiao, S.; Wei, Y.; Zhuo, Z.; Lin, Y.; Yang, W.; Xu, K.; Amine, K.; Pan, F. *Nano Lett.* **2015,** *15*, 5590-6.
38. Billinge, S. J. L.; Levin, I. *Science* **2007,** *316*, 561-565.
39. Keen, D. A.; Goodwin, A. L. *Nature* **2015,** *521*, 303-309.
40. Masadeh, A. S.; Bozin, E. S.; Farrow, C. L.; Paglia, G.; Juhas, P.; Billinge, S. J. L.; Karkamkar, A.; Kanatzidis, M. G. *Phys. Rev. B* **2007,** *76*.
41. Petkov, V.; Billinge, S. J.; Heising, J.; Kanatzidis, M. G. *J. Am. Chem. Soc.* **2000,** *122*, 11571-11576.
42. Hong, J.; Lim, H. D.; Lee, M.; Kim, S. W.; Kim, H.; Oh, S. T.; Chung, G. C.; Kang, K. *Chem. Mater.* **2012,** *24*, 2692-2697.
43. Koga, H.; Croguennec, L.; Menetrier, M.; Douhil, K.; Belin, S.; Bourgeois, L.; Suard, E.; Weill, F.; Delmas, C. *J. Electrochem. Soc.* **2013,** *160*, A786-A792.

44. Koga, H.; Croguennec, L.; Menetrier, M.; Mannessiez, P.; Weill, F.; Delmas, C. *J. Power Sources* **2013,** *236*, 250-258.
45. Li, W.; Reimers, J. N.; Dahn, J. R. *Phys. Rev. B* **1992,** *46*, 3236-3246.
46. Reed, J.; Ceder, G.; Van der Ven, A. *Electrochem. Solid-State Lett.* **2001,** *4*, A78-A81.
47. Kim, S.; Ma, X. H.; Ong, S. P.; Ceder, G. *Phys. Chem. Chem. Phys.* **2012,** *14*, 15571-15578.
48. Hu, E. Y.; Bak, S. M.; Liu, Y. J.; Liu, J.; Yu, X. Q.; Zhou, Y. N.; Zhou, J. G.; Khalifah, P.; Ariyoshi, K.; Nam, K. W.; Yang, X. Q. *Adv. Energy Mater.* **2016**, 6.
49. Yu, X.; Hu, E.; Bak, S.; Zhou, Y. N.; Yang, X. Q. *Chin. Phys. B* **2016**, 25.
50. Yu, X. Q.; Lyu, Y. C.; Gu, L.; Wu, H. M.; Bak, S. M.; Zhou, Y. N.; Amine, K.; Ehrlich, S. N.; Li, H.; Nam, K. W.; Yang, X. Q. *Adv. Energy Mater.* **2014**, 4.
51. Boulineau, A.; Simonin, L.; Colin, J. F.; Bourbon, C.; Patoux, S. *Nano Lett.* **2013,** *13*, 3857-3863.
52. Bloom, I.; Trahey, L.; Abouimrane, A.; Belharouak, I.; Zhang, X.; Wu, Q.; Lu, W.; Abraham, D. P.; Bettge, M.; Elam, J. W.; Meng, X.; Burrell, A. K.; Ban, C.; Tenent, R.; Nanda, J.; Dudney, N. *J. Power Sources* **2014,** *249*, 509-514.
53. Martha, S. K.; Nanda, J.; Kim, Y.; Unocic, R. R.; Pannala, S.; Dudney, N. J. *J. Mater. Chem. A* **2013,** *1*, 5587-5595.
54. Zheng, F.; Yang, C.; Xiong, X.; Xiong, J.; Hu, R.; Chen, Y.; Liu, M. *Angew. Chem. Int. Ed.* **2015,** *54*, 13058-13062.
55. Myung, S. T.; Izumi, K.; Komaba, S.; Sun, Y. K.; Yashiro, H.; Kumagai, N. *Chem. Mater.* **2005,** *17*, 3695-3704.
56. Sun, Y. K.; Lee, M. J.; Yoon, C. S.; Hassoun, J.; Amine, K.; Scrosati, B. *Adv. Mater.* **2012,** *24*, 1192-1196.

TOC Figure:

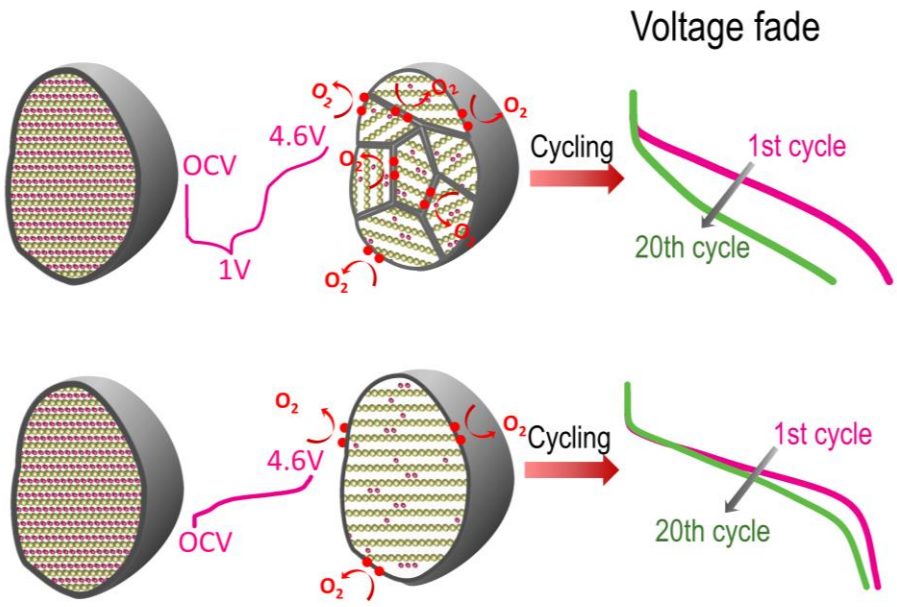
Voltage fade
OCV
4.6V
1V
Cycling
1st cycle
20th cycle
OCV
4.6V
Cycling
1st cycle
20th cycle